Journal of Catalysis 337 (2016) 293–302

Contents lists available at ScienceDirect

Journal of Catalysis

journal homepage: www.elsevier.com/locate/jcat

CO_2 photoreduction with H_2O vapor on highly dispersed CeO_2/TiO_2 catalysts: Surface species and their reactivity

Yun Wang [a,b], Jie Zhao [a,*], Tianfu Wang [a], Yingxuan Li [a], Xiyou Li [a,*], Jiao Yin [a], Chuanyi Wang [a,*]

[a] Laboratory of Environmental Sciences and Technology (LEMST), Xinjiang Technical Institute of Physics and Chemistry, Key Laboratory of Functional Materials and Devices for Special Environments, Chinese Academy of Sciences, Urumqi, Xinjiang 830011, China
[b] University of Chinese Academy of Sciences, Beijing 100049, China

ARTICLE INFO

Article history:
Received 7 November 2015
Revised 29 December 2015
Accepted 30 December 2015
Available online 2 March 2016

Keywords:
CO_2 photoreduction
Basic oxide
CeO_2
CO_2 adsorption

ABSTRACT

Weak interaction between TiO_2 and CO_2 molecules is detrimental to CO_2 photoreduction. To alleviate this drawback, ceria is usually exploited as a basic promoter, but fundamental insights into the correlation of ceria-tuned CO_2 adsorption and the resulting activity of photoreduction are lacking. In this work, highly dispersed CeO_2/TiO_2 and bare TiO_2 catalysts were fabricated and their structural, surface, and optical properties and activity for CO_2 photoreduction were explored. Microcalorimetric measurement and in situ infrared spectroscopy were used to reveal the strengths and states of CO_2 adsorption and the course of photoreduction of CO_2 with H_2O vapor. Monodentate carbonate (m-CO_3^{2-}), bidentate carbonate (b-CO_3^{2-}), and bidentate bicarbonate (b-HCO_3^-) are found to be the main surface species for the coadsorption of CO_2 and H_2O on catalyst surfaces. The presence of CeO_2 containing Ce^{3+} strengthens the bonding of CO_2 with catalyst surfaces and increases the production of b-CO_3^{2-} and b-HCO_3^- species. Unlike m-CO_3^{2-}, b-CO_3^{2-} and b-HCO_3^- surface species could readily be transformed to surface CO_2^- in the presence of H_2O under simulated sunlight irradiation. This might be attributed to the fact that the CO_2 segment in the two species is bound to Ti/Ce atoms that have reductive capabilities under photoirradiation. In addition, the presence of CeO_2 containing Ce^{3+} facilitates photogenerated charge separation. As a result, ceria-tuned CO_2 adsorption and enhanced charge separation are jointly responsible for the increased activity of CeO_2/TiO_2 catalysts.

© 2016 Elsevier Inc. All rights reserved.

1. Introduction

Photocatalytic reduction of CO_2 with H_2O vapor on chemically stable and environmentally benign TiO_2 is gaining increased interest because it is a promising "green chemistry" approach for the direct conversion of CO_2 to value-added fuels (CO, methane, methanol, etc.) driven by sunlight [1–3]. However, TiO_2 photocatalyst suffers from several disadvantages that ultimately lead to low reaction efficiency [4], including (1) low solar energy utilization due to its large band gap (3.2 eV for anatase TiO_2 and 3.0 for rutile TiO_2), (2) fast recombination of photogenerated electron–hole pairs, and (3) weak interaction between CO_2 molecules and TiO_2 surfaces, leading to low coverage of reactive adsorbed species and difficult displacement of the reaction products and/or inactive intermediates by CO_2 molecules [3]. The former two limitations have been extensively addressed in the literature by metal (e.g., Pt, Au) coupling or nonmetal doping, mixed phase TiO_2 [5,6], p–n heterojunction construction, photosensitizer decoration, and defect production [7,8]. However, limited attention has been focused on the last one, which is also a key factor in CO_2 photoreduction efficiency [3,9–12].

The surface chemistry of CO_2 suggests that two types of surface species for the adsorption of CO_2 exist on the surface of TiO_2, molecularly adsorbed CO_2 and surface carbonates [13,14]. They are easily desorbed from the clean and hydrated TiO_2 surfaces at room temperature due to low adsorption energy [13,15]. Recently, the use of basic additives to improve CO_2 adsorption has attracted some attention due to the fact that CO_2 is an acidic molecule [4]. Indeed, it has been found that alkali and alkaline earth metal additives such as MgO, Na_2CO_3, and NaOH exhibit positive effects on the photoreduction of CO_2 [3,9,10,16]. Meng et al. pointed out the modification of TiO_2 with NaOH can promote CO_2 chemisorption and subsequent activation, thereby resulting in highly effective conversion of CO_2 to CH_4 [9]. Rare earth metal oxides have been widely investigated as basic promoters. Besides promoting the adsorption of CO_2 [4,17], their addition could also provide several other benefits: (1) extending the light absorption of

* Corresponding authors. Fax: +86 9913838957 (C. Wang).
E-mail addresses: Jiezhao@ms.xjb.ac.cn (J. Zhao), xiyouli@upc.edu.cn (X. Li), cywang@ms.xjb.ac.cn (C. Wang).

http://dx.doi.org/10.1016/j.jcat.2015.12.030
0021-9517/© 2016 Elsevier Inc. All rights reserved.

TiO_2-based catalysts to the visible region [18,19], (2) promoting photogenerated electron–hole pair separation at ceria–titania interfaces [20–22], (3) increasing the redox capability [23], and (4) tailoring surface states of TiO_2 [24] Considering these factors, rare earth metal oxides could be promising promoters for CO_2 photoreduction on TiO_2.

Ceria is an important representative of rare earth metal oxides, and a lot of effort has been made to apply CeO_2–TiO_2 composites for photocatalytic oxidation of various organic pollutants such as dyes, toluene [25–27], pesticides, acetaldehyde, or 4-chlorophenol in condensed phase [28,29]. For example, Muñoz-Batista et al. have done systematic studies on photocatalytic degeneration of toluene over ceria–titania composites, revealing degeneration kinetics, the role of CeO_2–TiO_2 interface contact, and g-C_3N_4 modification effect [24–26]. Based on previous studies, it can be concluded that ceria–titania catalysts are advantageous in photocatalytic oxidation of organic pollutants, as compared to bare TiO_2. Unfortunately, little research regarding the photocatalytic reduction of CO_2 over CeO_2–TiO_2 photocatalysts has been reported, except for studies by Wang et al. [18], Matějová et al. [28], and Jiao et al. [30]. Wang et al. [18] and Jiao et al. [30] mainly focused on the preparation of ordered macro- and meso-porous CeO_2–TiO_2 materials and attributed enhanced CO_2 photoreduction performance to their special composition and structure. The work by Matějová et al. [28] indicated that the introduction of ceria to TiO_2 adjusted the energies of electrons and holes of the catalysts, thereby enhancing the CO_2 photoreduction activity. These three studies focused on the relationship between the structural/electronic properties of the CeO_2–TiO_2 catalyst and its CO_2 photoreduction activity. To the best of our knowledge, however, the fundamental role of ceria-tuned CO_2 adsorption in its photoreduction has not yet been investigated.

Interface plays an important role in catalytic reactions [22,24,31]; e.g., the presence of interfaces obviously facilitates photogenerated charge separation in photocatalysis. Reducing particle size can effectively increase the interfacial areas, thus achieving desirable catalytic activity [24]. In view of this, highly dispersed CeO_2 on TiO_2 catalysts were prepared by a one-pot hydrothermal method in this work. Their structural, surface, and optical properties and activity for CO_2 photoreduction were systematically studied. Microcalorimetric measurement and in situ infrared spectroscopy (IR) were used to reveal the strengths and states of CO_2 adsorption and the course of photoreduction of CO_2 with H_2O vapor. The presence of CeO_2 tuned adsorptive states of CO_2 on catalyst surfaces in the presence of H_2O, resulting in increased production of bidentate carbonate (b-CO_3^{2-}) and bidentate bicarbonate (b-HCO_3^-) relative to monodentate carbonate (m-CO_3^{2-}) (shown in Scheme 1). The two surface species could be readily transformed to surface CO_2^- under simulated sunlight irradiation, which is a key intermediate for CO_2 photoreduction. The present work deepens the understanding of the role of ceria in CO_2 photoreduction at TiO_2 catalysts and the course of catalysis of CO_2 photoreduction in the presence of H_2O vapor.

2. Experimental

2.1. Synthesis of photocatalysts

Highly dispersed CeO_2 on TiO_2 photocatalysts was prepared through a one-pot hydrothermal method using titanium (IV) bis (ammonium lactate) dihydroxides (TALH; AR, Alfa Aesar) as Ti source and $Ce(NO_3)_3{\cdot}6H_2O$ (AR; Aladdin) as Ce source, respectively. In detail, a desired amount of TALH and $Ce(NO_3)_3{\cdot}6H_2O$ was dissolved into 120 mL of distilled water in the presence of 0.1 g polyethylene glycol (PEG, M_w = 6000; AR, Aladdin). The solution was transferred to a 175 mL Teflon-lined stainless steel autoclave, which was sealed and placed in an electric oven under stirring at 250 °C for 2 h with a heating rate of 2 °C/min. The as-formed slurry was filtered and washed with distilled water. The filter cake was dried at 80 °C for 4 h and then annealed in air at 450 °C for 2 h. The as-prepared CeO_2/TiO_2 photocatalysts with CeO_2 10, 20, and 40 wt.% were denoted as 0.1 CeO_2/TiO_2, 0.2 CeO_2/TiO_2, and 0.4 CeO_2/TiO_2, respectively. For reference, the bare TiO_2 and CeO_2 were synthesized using the same method.

2.2. Photocatalyst characterization

The chemical compositions of prepared photocatalysts were analyzed by an ARL-9800 X-ray fluorescence spectrometer (XRF). The surface area and pore size were determined using an Autosorb-IQ-MP autosorption analyzer. Experiments were carried out at 77.3 K using N_2 as an adsorbate. The samples were degassed at 473 K for 2 h before the measurements. The pore size distributions were estimated by the BJH method using the desorption branch of the isotherms. X-ray diffraction (XRD) patterns of samples were collected in ambient atmosphere by a Bruker D8 powder diffractometer with Cu Kα radiation (λ = 1.5408 Å) generated at 40 kV and 30 mA. Diffraction intensities were recorded from 20° to 80° at a rate of 6°/min. Transmission electron microscopy (TEM) characterization was performed on a JEOL-JEM 2100 electron microscope. X-ray photoelectron spectroscopy (XPS) was performed using a VG Microtech MT500 with an Mg Kα X-ray source. The binding energy scale was corrected for surface charging using the C1*s* peak of contaminant carbon as a reference at 285.6 eV.

The UV–vis diffuse reflectance spectra (DRS) of photocatalysts over the range 200–800 nm were obtained on a UV–vis spectrophotometer (ShimadzuSolidSpec-3700DUV) with an integration sphere diffuse reflectance attachment. The photocurrent experiments were performed in three-electrode quartz cells with 0.1 M Na_2SO_4 electrolyte solution. A platinum electrode was used as the counter electrode, and saturated calomel electrodes (SCE) were used as the reference electrodes. Working electrodes were prepared as follows: ITO glasses were washed sequentially with distilled water and ethanol in an ultrasonic cleaner for 30 min. A quantity of 10 mg of catalysts was fixed on the pretreated ITO glasses to form photocatalyst-modified ITO electrodes. A 300 W xenon lamp was used as light source, which was 15 cm away from the working electrode.

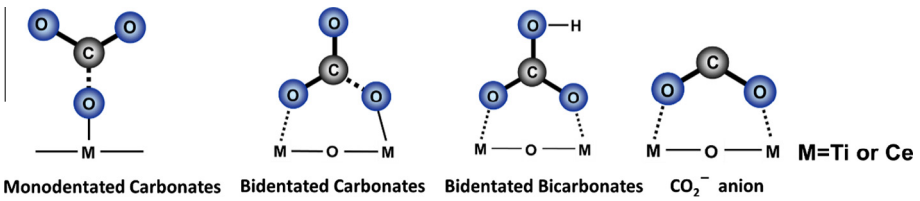

Scheme 1. Schematic diagram of surface species for the coadsorption of CO_2 and H_2O on TiO_2 and/or CeO_2 surfaces [52,57].

Microcalorimetric measurement for CO_2 adsorption was performed on a Tian–Calvet heat-flux apparatus. A C-80 calorimeter (Setaram, France) was connected to a volumetric system equipped with a Baratron capacitance manometer (USA) for pressure measurements and gas handling. Prior to the microcalorimetric measurements, the catalysts were treated in air at 473 K for 2 h, followed by evacuation at the same temperature for 1 h.

In situ IR spectra for the coadsorption of CO_2 and H_2O before and after simulated sunlight irradiation were recorded with a Nicolet (IS50) spectrophotometer (MCT detector) in the range 4000–1000 cm^{-1} with a resolution of 4 cm^{-1}. The self-supporting wafer (15–20 mg) was annealed in an IR cell at 473 K in Ar for 2 h and evacuated at the same temperature for 1 h. After the IR cell was cooled, CO_2 and H_2O vapor were introduced into the cell with or without evacuation.

2.3. Photoactivity tests

The photocatalytic reduction of CO_2 with H_2O vapor was carried out in a reactor connected with a mechanical vacuum pump, using a 300 W xenon lamp as light source. For each test, 10 mg of tested catalyst powder was evenly deposited on a circular quartz plate with a diameter of 50 cm and then located inside the photoreactor perpendicular to the light beam. Gaseous CO_2 at 8 kPa was produced in situ by the reaction of $NaHCO_3$ with a H_2SO_4 solution (0.5 M). The photocatalytic activity of reduction of CO_2 with H_2O was performed at 298 K for 6 h in each run. The reaction products were monitored at a 60 min interval by an online gas chromatograph (Agilent Technology 4890 GC) equipped with a thermal conductivity detector (TCD) for product analysis of O_2, CO, and CH_4 and a flame ionization detector (FID) for probable products of C_2–C_5 hydrocarbons and methanol.

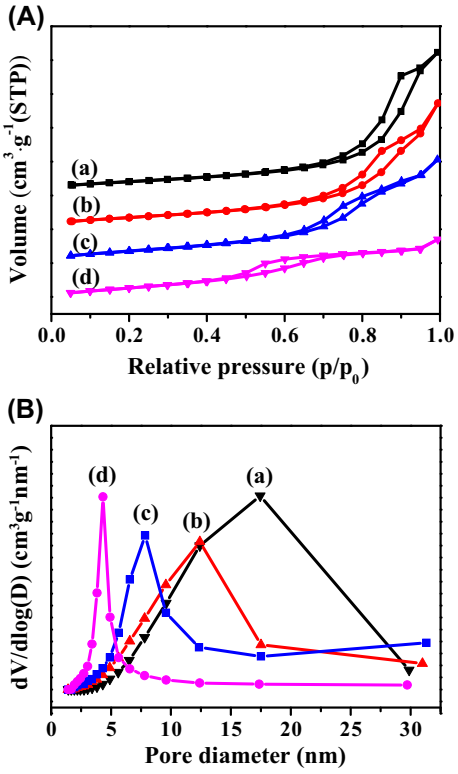

Fig. 1. N_2 adsorption–desorption isotherms (A) and pore size distribution curves (B) of the TiO_2 (a), 0.1 CeO_2/TiO_2 (b), 0.2 CeO_2/TiO_2 (c) and 0.4 CeO_2/TiO_2 (d) photocatalysts.

3. Results and discussion

3.1. Textural and structural properties

Fig. 1 shows the N_2 adsorption–desorption isotherms and pore size distribution curves of as-prepared TiO_2, 0.1 CeO_2/TiO_2, 0.2 CeO_2/TiO_2, and 0.4 CeO_2/TiO_2 photocatalysts. Their compositions, BET surface areas, and pore structure parameters are summarized in Table 1. All of the photocatalysts exhibit type-IV adsorption with a hysteresis loop of type H1, indicating the existence of mesopore structure. A relatively broad pore size distribution is observed for bare TiO_2, and it narrows down gradually as the CeO_2 content increases (shown in Fig. 1B). The surface area increases while pore diameter and pore volume decrease with increasing CeO_2 content. For example, surface area, pore diameter, and pore volume were measured to be 150.4 $m^2\ g^{-1}$, 17.4 nm, and 0.7 cm^3/g for TiO_2, whereas 196.1 $m^2\ g^{-1}$, 4.3 nm, and 0.3 cm^3/g were found for 0.4 CeO_2/TiO_2. Type and abundance of ions in hydrothermal processes have critical effects on the specific surface area, morphology, and particle size of as-prepared materials [32,33]; e.g., Cheng et al. found that mineralizer NH_4Cl can decrease the crystalline size of TiO_2 but promotes agglomeration to form a hairy spheroid of particles in hydrothermal synthesis [33]. In the present work, the formation of TiO_2 is prior to that of CeO_2 in the hydrothermal process due to the comparatively lower decomposition temperature for TALH. Thus, the NO_3^- and Ce^{3+} ions derived from $Ce(NO_3)_3$ ionization could be adsorbed onto the surface of TiO_2 crystal nuclei. If they were selectively adsorbed on certain facets of the crystal nuclei, TiO_2 crystallite particles with specific morphology would be obtained [33]. If the adsorption was not selective, the adsorbed ions would hinder the growth of TiO_2 crystal nuclei [34,35], leading to a higher specific surface area and smaller pore diameter of the resultant samples. Furthermore, $Ce(NO_3)_3$ can be hypothesized to distribute throughout the interior of the pores of TiO_2 and subsequently decompose to CeO_2, resulting in decreased pore volume. Based on these analyses, the observed trends in specific surface area, pore diameter, and pore volume could be ascribed to the presence of $Ce(NO_3)_3$.

Table 1
Physical properties of the TiO_2, 0.1 CeO_2/TiO_2, 0.2 CeO_2/TiO_2, and 0.4 CeO_2/TiO_2 photocatalysts.

Photocatalyst	Composition (wt.%)		S_{BET} (m^2/g)[a]	V_p (cm^3/g)[b]	Most probable pore size (nm)	Diameter (nm)[c]
	CeO_2	TiO_2				TiO_2
TiO_2	0	100	150.4	0.7	17.4	6.5
0.1 CeO_2/TiO_2	8.7	91.3	161.7	0.6	12.4	6.4
0.2 CeO_2/TiO_2	18.0	82.0	195.9	0.5	7.8	4.7
0.4 CeO_2/TiO_2	37.2	62.8	196.1	0.3	4.3	–[d]

[a,b] S_{BET} and V_p represent specific surface area and pore volume, respectively.
[c] Particle size of TiO_2 as calculated according to Scherrer's equation.
[d] Not calculated.

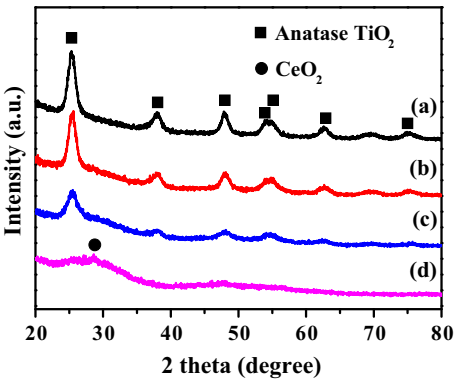

Fig. 2. XRD patterns of the TiO_2 (a), 0.1 CeO_2/TiO_2 (b), 0.2 CeO_2/TiO_2 (c) and 0.4 CeO_2/TiO_2 (d) photocatalysts calcined at 450 °C in air.

Fig. 2 shows XRD patterns of TiO_2, 0.1 CeO_2/TiO_2, 0.2 CeO_2/TiO_2, and 0.4 CeO_2/TiO_2. The diffraction peaks of 2θ at 25.3°, 37.8°, 40.8°, 53.9°, 55.1°, 62.7° and 75.1° are assigned to the (101), (004), (200), (105), (211), (204), and (219) crystal faces of anatase TiO_2, respectively [24]. Their intensities decrease with decreasing TiO_2 content in the CeO_2/TiO_2 catalysts. Based on the Scherrer equation using the (101) diffraction peak of TiO_2 anatase at 25.6°, the average crystallite size of anatase TiO_2 is calculated to be 6.5, 6.4, and 4.7 nm for TiO_2, 0.1 CeO_2/TiO_2, and 0.2 CeO_2/TiO_2, respectively. The characteristic peaks of crystalline CeO_2 are not observed for 0.1 CeO_2/TiO_2, 0.2 CeO_2/TiO_2, or 0.4 CeO_2/TiO_2, except for a very weak peak at 28.6° for 0.4 CeO_2/TiO_2. To examine if CeO_2 is amorphous, bare CeO_2 was prepared by the same method and analyzed by XRD. Strong diffraction peaks for cubic fluorite CeO_2 with an average diameter of 29 nm are observed, indicating that crystalline CeO_2 can be obtained under the present preparation condition (Fig. S1 in the Supporting Information). It is well accepted that if the size of crystalline particles decreases to 4 nm, their diffraction peaks will be significantly broadened or even disappear [11]. On the other hand, it was reported that CeO_2 very likely displayed amorphous-like structure once the particle size was decreased to a certain extent [36]. A similar case was observed for metallic Cu particles [18]. Therefore, it could be assumed that the disappearing diffraction peaks are attributable to the small size of CeO_2 particles in CeO_2/TiO_2. Moreover, the particle size of CeO_2 in CeO_2/TiO_2 hybrids is significantly smaller than that in bare CeO_2, suggesting that TiO_2 has strong dispersion effects on CeO_2. In other words, CeO_2 is highly dispersed on TiO_2.

The TEM and HRTEM images of the representative photocatalyst 0.4 CeO_2/TiO_2 are shown in Fig. 3. As shown in Fig. 3A, spherical CeO_2/TiO_2 composite particles are observed with an average diameter of about 8 nm. The HRTEM image displays the crystalline fringes with an interplanar spacing of 0.35 nm, corresponding to the (101) plane of anatase TiO_2 crystal (Fig. 3B). Some studies showed that anatase TiO_2 is formed under weakly acidic, neutral, or basic conditions, while rutile TiO_2 is a main hydrothermal product under strongly acidic conditions [32]. Hence, the anatase TiO_2 was formed in the present work due to the weakly acidic experimental conditions. Furthermore, it is difficult to find the fringes for the cubic fluorite CeO_2, evidencing amorphous-like structure for CeO_2, attributed to the small size of CeO_2 particles.

3.2. XPS analysis

Fig. 4 shows Ti2*p*, Ce3*d*, and O1*s* core levels XPS spectra of TiO_2, 0.1 CeO_2/TiO_2, 0.2 CeO_2/TiO_2, 0.4 CeO_2/TiO_2, and CeO_2 photocatalysts. No impurities other than contaminant carbon were detected (Fig. S2 in the Supporting Information). The binding energies of

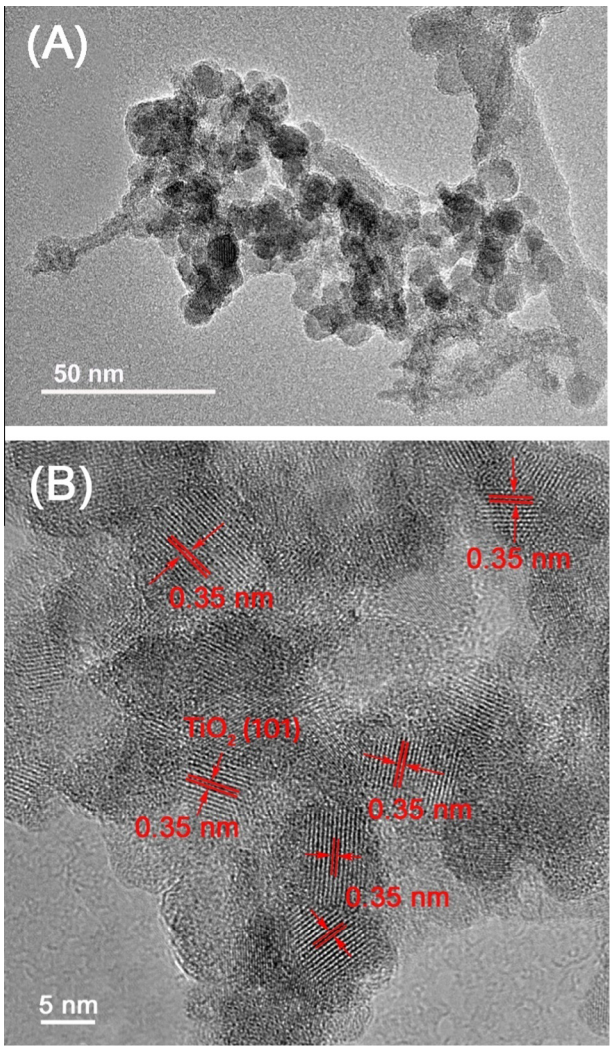

Fig. 3. (A) TEM and (B) HRTEM images of the 0.4 CeO_2/TiO_2 photocatalyst.

Ti2$p_{3/2}$ and 2$p_{1/2}$ in TiO_2 are 458.4 and 464.4 eV (Fig. 4A), corresponding to typical characteristics of octahedrally coordinated Ti^{4+} ions [37]. The presence of CeO_2 does not change the Ti2*p* binding energies, in agreement with Liu et al. [29]. In addition, the binding energies for Ti^{3+}2*p* core levels are only about 1.5 eV lower than those for Ti^{4+}2*p* core levels [38], and thus their photoemission peaks often overlap. To examine if Ti^{3+} was present on the surface of TiO_2, 0.1 CeO_2/TiO_2, 0.2 CeO_2/TiO_2, and 0.4 CeO_2/TiO_2 photocatalysts, deconvolution of the peaks at 458.4 and 464.4 eV was tried but failed. This suggests that the amount of Ti^{3+} on the surface of photocatalysts is very limited.

As shown in Fig. 4B, Ce3*d* spectra are composed of two multiplets, labeled v and u, corresponding to the spin–orbit coupling of 3$d_{5/2}$ and 3$d_{3/2}$ [19,22,24,39]. The peaks denoted as v (u), v″ (u″), and v‴ (u‴) are related to the photoemission from the Ce^{4+}3*d* core level with Ce3$d^9$4f^2O2p^4, Ce3$d^9$4f^1O2p^5, and Ce3$d^9$4f^0O2p^6 final states, respectively. The transfer of electrons from O2*p* to Ce4*f* orbitals in the photoemission would increase the electron density of Ce^{4+}, thus decreasing the attraction of the Ce nucleus to extranuclear electrons while enhancing the repulsion between electrons. This is why the binding energies for the Ce^{4+}3*d* core level are decreased with the increased number of transferred electrons from O2*p* orbitals. The signals v_0 (u_0) and v′ (u′) are ascribed to photoemission from Ce^{3+} cations [22,40]. Based on these observations, it could be concluded that a mixture of Ce^{3+}/Ce^{4+} oxidation

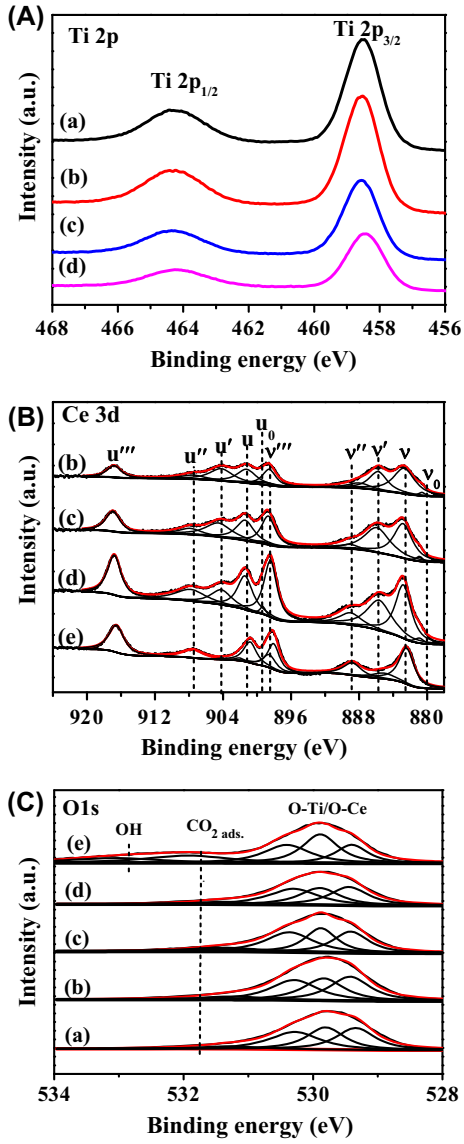

Fig. 4. (A) Ti 2p, (B) Ce 3d and (C) O 1s core level XPS spectra of the TiO_2 (a), 0.1 CeO_2/TiO_2 (b), 0.2 CeO_2/TiO_2 (c), 0.4 CeO_2/TiO_2 (d) and CeO_2 (e) photocatalysts.

states exists on the surface of the CeO_2/TiO_2 catalysts, which is also revealed by the studies of Luo et al. [22]. In addition, based on the intensities of $Ce^{3+}3d$ photoemission peaks, the quantity of Ce^{3+} on the surface of CeO_2/TiO_2 catalysts is deemed to increase with the increase in CeO_2 content.

O1*s* XPS spectra are shown in Fig. 4C. The single O1*s* peak can be resolved into five peaks at about 529.3, 529.8, 530.3, 531.7, and 532.9 eV. The three peaks between 528 and 530.5 eV can be assigned to oxygen in anatase TiO_2 and/or CeO_2 crystal lattices [41,42]. The peaks between 531 and 533 eV correspond to the surface-adsorbed oxygen. The peak at 532.9 eV can be attributed to OH species [42]. The peak at about 531.2 eV could be ascribed to the oxygen in adsorbed CO_2, which is the most intense for bare CeO_2 due to its strong alkalinity.

The atomic fractions of Ti, Ce, and O on the surfaces of pure TiO_2, CeO_2, and CeO_2/TiO_2 catalysts derived from the deconvolution of XPS spectra are summarized in Table 2. The atomic fraction of oxygen on the surfaces of photocatalysts is higher than the theoretical value 66.7% for TiO_2 and CeO_2, which is likely due to the presence of adsorbed oxygen. The concentration of Ce^{3+} relative

Table 2
Summary of the XPS data for the TiO_2, 0.1 CeO_2/TiO_2, 0.2 CeO_2/TiO_2, and 0.4 CeO_2/TiO_2 photocatalysts.

Samples	Surface atomic concentration (%)			Ce species (%)	
	Ti	Ce	O	Ce^{3+}	Ce^{4+}
TiO_2	29.7	0	70.3	–[a]	–[a]
0.1 CeO_2/TiO_2	25.8	4.0	70.2	33.1	66.9
0.2 CeO_2/TiO_2	23.5	6.4	70.1	35.0	65.0
0.4 CeO_2/TiO_2	19.9	10.5	69.6	25.8	74.2
CeO_2	–[a]	20.6	79.4	14.8	85.2

[a] Not detected.

to the combination of Ce^{4+} and Ce^{3+} is 33.1%, 35.0%, 25.8%, and 14.8% for 0.1 CeO_2/TiO_2, 0.2 CeO_2/TiO_2, 0.4 CeO_2/TiO_2, and CeO_2, respectively. Theoretical and experimental studies by Johnston-Peck et al. and Muñoz-Batista et al. showed that the ceria–titania interface favors the stabilization of Ce^{3+} [22,24,43,44], which could explain the reason that the Ce^{3+} ratio of CeO_2/TiO_2 hybrids is significantly higher than that of bare CeO_2 in the present work.

3.3. Optical properties

Fig. 5 displays the UV–vis diffuse reflectance spectra for as-prepared TiO_2, 0.1 CeO_2/TiO_2, 0.2 CeO_2/TiO_2, and 0.4 CeO_2/TiO_2. TiO_2 is shown to have no significant absorption for visible light, owing to its large energy gap. However, the addition of CeO_2 extends the absorption of the resulting photocatalysts to visible light with the wavelength of 500 nm, which is also observed in previous reports [22,29,45]. This phenomenon can be attributed to the presence of reduced species such as Ce^{3+}, as evidenced by XPS analysis. It is necessary here to elaborate the energy band structure of CeO_2 based on the theoretical calculations. CeO_2 has three valence bands, which are mainly composed of O2*p*, Ce4*f*, and Ce5*d* states

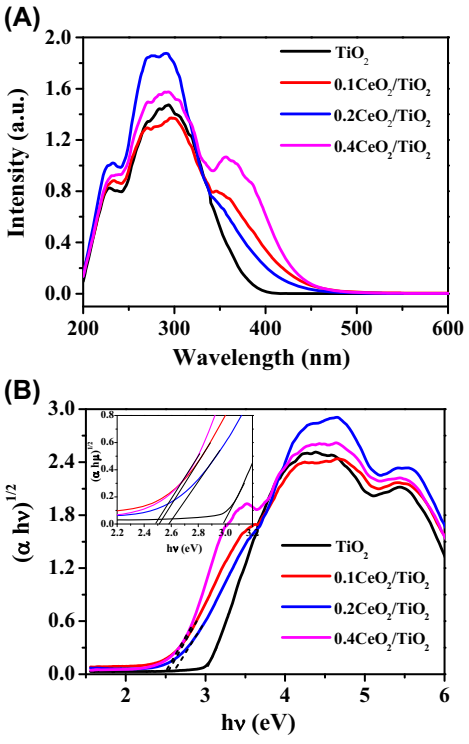

Fig. 5. (A) UV–vis diffuse reflectance spectra and (B) the optical adsorption edges of the TiO_2, 0.1 CeO_2/TiO_2, 0.2 CeO_2/TiO_2 and 0.4 CeO_2/TiO_2 photocatalysts.

[45]. The *p–f* and *p–d* band gaps exceed 3.1 eV, thus requiring ultraviolet light excitation. Although the *f–d* band gap energy of CeO_2 is about 2.4 eV [46–48], there is no visible-light absorption by pure CeO_2, due to the fact that the 4*f* orbital of Ce^{4+} is unoccupied. The presence of Ce^{3+} in CeO_2 will induce occupation of the 4*f* orbitals, thus allowing visible-light absorption via the transition of electrons from 4*f* to 5*d* orbitals. In addition, the intensities of visible-light absorption of CeO_2/TiO_2 hybrids should increase with Ce^{3+} quantity. However, it is found that visible-light absorption of 0.2 CeO_2/TiO_2 is weaker than that of 0.1 CeO_2/TiO_2. The abnormal observation is tentatively attributed to the specific composition, which might change the electron structure of Ce^{3+} in 0.2 CeO_2/TiO_2 [28], thus slightly enlarging the *f–d* band gap.

The energy band gap of as-prepared samples could be calculated using $(\alpha h\nu)^n = \kappa(h\nu - E_g)$, (where α is the absorption coefficient, κ is a parameter that is related to the effective masses associated with the valence and conduction bands, n is 1/2 for the direct transition, $h\nu$ is the absorption energy, and E_g is the band gap energy) [31]. Plotting $(\alpha h\nu)^{1/2}$ versus $h\nu$ based on the spectral response in Fig. 5A gives the extrapolated intercept corresponding to the E_g value, and the results are shown in Fig. 5B. The optical band energies of 0.1 CeO_2/TiO_2, 0.2 CeO_2/TiO_2, and 0.4 CeO_2/TiO_2 are calculated to be 2.52, 2.6, and 2.51 eV, respectively, lower than that of TiO_2 (2.98 eV), indicating the enhanced ability of the hybrid catalysts to absorb visible light.

To explore the separation efficiency of photoinduced electron–hole pairs in the photocatalysts, transient photocurrent measurements were conducted, with the results being shown in Fig. 6. Each electrode exhibits a current response to light, and the current decreases rapidly as soon as the light is off. The photocurrent density is about 0.029 μA cm^{-2} for TiO_2 and increases after the addition of CeO_2. CeO_2 and TiO_2 have almost equivalent conduction band potential [19], while the valance band potential of CeO_2 is higher than that of TiO_2, according to theoretical calculations [46–48]. The presence of CeO_2 containing Ce^{3+} produces a new valance band-occupied 4*f* orbitals with the potential lower than that of TiO_2, as shown in Scheme 2 [22,45,30]. Consequentially, photogenerated holes of TiO_2 could readily be transferred to CeO_2 through ceria–titania interfaces, leading to spatial separation of the photogenerated charge carriers, thereby increasing electron lifetimes [22,30]. In addition, the photocurrent density increases with an increase in CeO_2 content and reaches a maximum at 20 wt.%. After that, it decreases with further increasing CeO_2 content. A similar phenomenon was also observed by Luo et al. [22], which was explained in terms of ceria–titania interfacial areas [24].

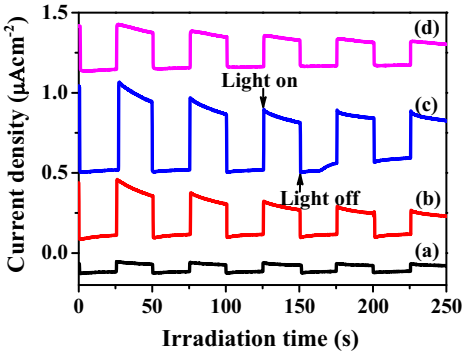

Fig. 6. Transient photocurrent curves for TiO_2 (a), 0.1 CeO_2/TiO_2 (b), 0.2 CeO_2/TiO_2 (c) and 0.4 CeO_2/TiO_2 (d) in Na_2SO_4 aqueous solution (0.1 M) under simulated sunlight at −0.500 V vs. saturated calomel electrode (SCE).

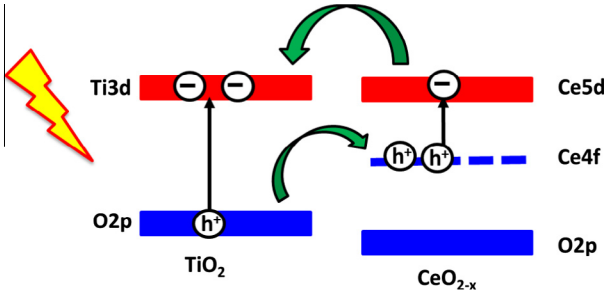

Scheme 2. Possible transfer of photogenerated charge carries at the ceria–titania interface under simulated solar light irradiation [22,45,48].

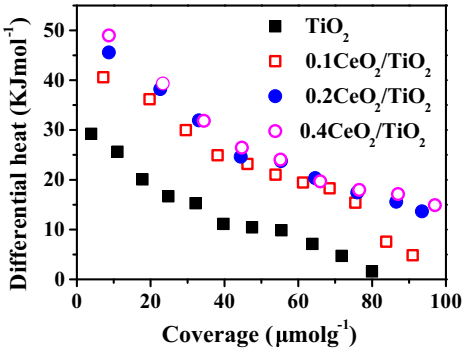

Fig. 7. Differential heat versus coverage for CO_2 adsorption at 300 K on the TiO_2, 0.1 CeO_2/TiO_2, 0.2 CeO_2/TiO_2 and 0.4 CeO_2/TiO_2 photocatalysts. Before measurements, the photocatalysts were calcined at 200 °C under vacuum.

3.4. Microcalorimetric adsorption and in situ FTIR studies

Microcalorimetric adsorption is a powerful tool for analyzing the interaction between reactants and catalyst surfaces [11,49]. Fig. 7 shows the results of microcalorimetric measurements for CO_2 adsorption on the surface of photocatalysts. The initial differential heat was measured to be about 29, 40, 45, and 49 kJ/mol on TiO_2, 0.1 CeO_2/TiO_2, 0.2 CeO_2/TiO_2, and 0.4 CeO_2/TiO_2, respectively. The differential heat decreases with an increase in CO_2 coverage on the surface of photocatalysts. Moreover, it is clear that the differential heat vs. coverage curves are gradually raised with the increase of CeO_2 content. These results indicate that the presence of CeO_2 containing Ce^{3+} strengthens the interaction between photocatalyst surfaces and CO_2 molecules, and the degree of strengthening depends on the quantity of Ce^{3+} on the surfaces of photocatalysts, as indicated by XPS analysis. This is due to the fact that the Ce^{3+} has excess electrons localized in empty *f* orbitals, thus possessing relatively stronger basicity than CeO_2 and TiO_2 [50].

Fig. 8 displays in situ FTIR spectra for the coadsorption of CO_2 and H_2O on the surface of TiO_2 and 0.2 CeO_2/TiO_2 photocatalysts before and after simulated solar light irradiation. As for the coadsorption of CO_2 and H_2O on TiO_2 in the dark, four infrared (IR) peaks are observed at 1605, 1515, 1392, and 1342 cm^{-1}. The peaks at 1605 and 1342 cm^{-1} can be assigned to the asymmetric and symmetric OCO stretches of bidentate carbonates (b-CO_3^{2-}), respectively [3,51–53]. Note that the 1605 cm^{-1} peak is very broad, implying the possible existence of other surface species such as bidentate bicarbonate (b-HCO_3^-) with an IR absorption band at about 1629 cm^{-1}, as reported previously [53,54]. The peaks at 1510 and 1392 cm^{-1} correspond to the asymmetric and symmetric OCO stretches of m-CO_3^{2-} [51,53]. Comparing the IR spectra for the coadsorption of CO_2 and H_2O on 0.2 CeO_2/TiO_2 with those on TiO_2 in the dark, several differences are observed:

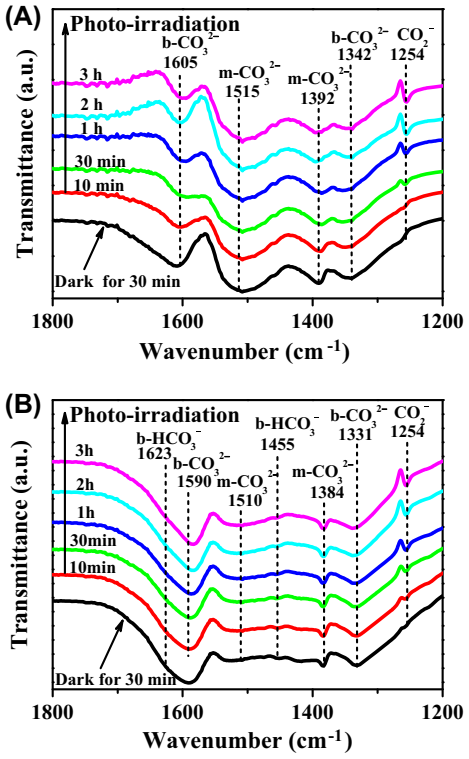

Fig. 8. In situ FTIR spectra for coadsorption of a 1:1 flux ratio mixture of CO_2 and H_2O vapor on TiO_2 (A) and 0.2 CeO_2/TiO_2 (B). The spectra were obtained after the exposure of TiO_2 and 0.2 CeO_2/TiO_2 at room temperature to CO_2 and H_2O vapor before and after simulated solar light irradiation.

(1) The above-mentioned four peaks are red-shifted for the hybrid catalyst. For example, the band for asymmetric OCO stretches of b-CO_3^{2-} shifts to 1590 cm^{-1}. As shown in Scheme 1, the CO_2 molecule is bonded to the surface oxygen atom of TiO_2 through its carbon atom, leading to the formation of surface m-CO_3^{2-} species [55]. If CO_2 is simultaneously bonded to the oxygen and Ti centers of TiO_2 through its carbon and oxygen, surface b-CO_3^{2-} species will be formed. In the two adsorption structures, the CO_2 molecule accepts electrons from the surfaces, and the accepted electrons mainly occupy the lowest unoccupied molecular orbital (LUMO) of CO_2 molecules with anti-bonding characteristics [56]. Thus, the more transferred electrons, the weaker OCO stretches and the stronger adsorption bond. The addition of ceria to TiO_2 could enhance the basicity and electron density of the catalyst surfaces, thereby weakening OCO stretching vibration but strengthening interaction between CO_2 and catalyst surfaces [56]. This is in agreement with the results of microcalorimetric measurements for the adsorption of CO_2. It should be noted that the surface species for the adsorption of CO_2 on CeO_2 is similar to those on TiO_2 [57–59].

(2) A distinguishable IR absorption band for b-HCO_3^- species is observed at about 1623 cm^{-1}. The surface b-HCO_3^- species is generated from the reaction of CO_2 and surface hydroxyls, which is derived from the dissociative adsorption of H_2O on the surfaces [52,60,61]. b-HCO_3^- could be readily formed on the surface of 0.2 CeO_2/TiO_2, since the dissociative adsorption of H_2O is facilitated on basic surfaces [61]. For bare CeO_2 (Fig. S3 in the Supporting Information), m-CO_3^{2-}, b-CO_3^{2-}, and b-HCO_3^- are the main surface species, similar to those on TiO_2 and 0.2 CeO_2/TiO_2. However, the production of b-HCO_3^- is higher than that of m-CO_3^{2-} and b-CO_3^{2-}, further suggesting that basic surfaces facilitate the reaction of CO_2 with H_2O.

(3) The main surface species is changed from m-CO_3^{2-} on TiO_2 to b-CO_3^{2-} and b-HCO_3^- on 0.2 CeO_2/TiO_2. Compared with m-CO_3^{2-}, the b-CO_3^{2-} species has additional bonding between the oxygen in the CO_2 molecule and the metal center of oxides, as suggested in Scheme 1. It is well known that the binding of the oxygen in the CO_2 molecule to the coordinately unsaturated metal center is energetically favorable. The presence of Ce^{3+} on the surface of CeO_2 and at the interface would lead to coordinatively unsaturated Ce centers, thus facilitating the formation of b-CO_3^{2-}.

Under subsequent photoillumination, a new IR peak at 1254 cm^{-1} appears for both bare TiO_2 and CeO_2/TiO_2 catalysts, which can be assigned to the symmetric OCO stretching of carbonate (CO_2^-). Specifically, the CO_2^- species on TiO_2 and CeO_2/TiO_2 catalysts is initially observed after 30 and 10 min of photoirradiation, respectively. With further increasing photoillumination time, the amount of CO_2^- species gradually increases and holds steady after 2 h photoillumination. At the same time, a very weak peak at about 2144 cm^{-1} for CO was monitored on the surface of 0.2 CeO_2/TiO_2 (shown in Fig. S2). The CO_2^- species was theoretically and experimentally verified by several research groups, with the possible configuration being shown in Scheme 1 [1,37,56,62]. Zhao et al. found that CO_2^- species could be formed in the coadsorption of CO_2 with H_2O on the surface of TiO_2 without photoillumination [37]. Liu et al. suggested that the formation of CO_2^- species depends on the surface properties of TiO_2 [1]. Combining our results, it could be assumed that the formation of CO_2^- surface species on catalyst surfaces is facilitated by photoillumination [62]. Moreover, the CO_2^- species is deemed to be a key intermediate in the photoreduction of CO_2. Based on theoretical analysis, when one of the C–O bonds in CO_2^- is cleaved to form C–Ti bonds, CO is then formed [63]. If CO_2^- is bonded to H on the surface, HCOOH is produced [63]. CH_4 is an ultimate product for CO_2 photoreduction, requiring multistep reduction. As such, CH_4 might be derived from intermediate products such as CO, HCOOH, CH_2O, or CH_3OH. Unfortunately, the characteristic IR peaks for HCOOH, CH_2O, CH_3OH, and CH_4 were not detected, likely due to low abundance of these products, with concentrations below the detection limit of FTIR instrumentation. It should be kept in mind that the reduction potential of electrons in the TiO_2 conduction band (≈−0.5 V) is much lower than the theoretical thermodynamic requirements for the reduction of CO_2 to CO_2^- (−1.9 V) [2]. Thus, the observed CO_2^- on the surfaces of TiO_2 and 0.2 CeO_2/TiO_2 should not be directly derived from gaseous or physisorbed CO_2 molecules. Furthermore, the peak intensities of b-CO_3^{2-} and b-HCO_3^- decrease slightly with photoillumination time. If surface b-CO_3^{2-} and b-HCO_3^- are directly transformed to the gaseous products such as CO, CO_2 in the IR cell will be readsorbed onto liberated sites to form b-HCO_3^- and b-CO_3^{2-} species, and thus the peak intensities for them remain stable, in contrast to our observations. Based on this, it is speculated that b-HCO_3^- and b-CO_3^{2-} on the surface are transformed to surface CO_2^- species instead.

To verify this speculation, another infrared analysis for the coadsorption of CO_2 and H_2O on the surface of the 0.2 CeO_2/TiO_2 photocatalyst was conducted. The experimental conditions are the same as in the above experiments, except that the IR cell was evacuated for 30 min after the exposure to CO_2 and H_2O vapor, which aims to remove the gaseous and physisorbed CO_2 and H_2O molecules. As shown in Fig. 9, the surface species on the surface of the 0.2 CeO_2/TiO_2 photocatalyst are not changed by evacuation. When the photoirradiation time is increased from 1 to 3 h, the peak intensities for b-HCO_3^- and b-CO_3^{2-} gradually decrease, while the peak intensity for CO_2^- increases. The peak at 1388 cm^{-1} assigned to symmetric OCO stretches of surface m-CO_3^{2-} species shows little change. The results indicate that both the b-HCO_3^- and b-CO_3^{2-} species can be converted to the surface CO_2^- species [64], while

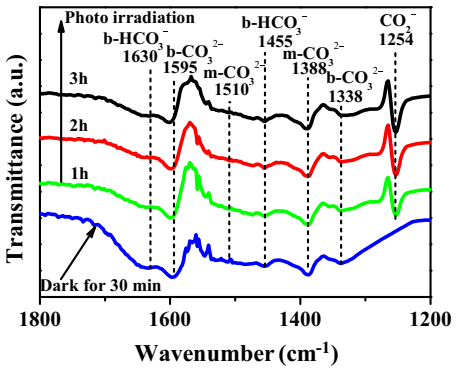

Fig. 9. In situ FTIR spectra for coadsorption of a 1:1 flux ratio mixture of CO_2 and H_2O vapor on 0.2 CeO_2/TiO_2. The spectra were obtained after the exposure of 0.2 CeO_2/TiO_2 at room temperature to CO_2 and H_2O vapor followed by evacuation for 30 min before and after simulated solar light irradiation.

the m-CO_3^{2-} species is inactive under simulated sunlight irradiation. The valence and conduction bands of TiO_2 (or CeO_2) are mainly composed of O2*p* and Ti3*d* (or Ce5*d*) orbitals, respectively. Note that 4*f* orbitals could also be regarded as a valence band for CeO_2 containing Ce^{3+}. Photogenerated holes with oxidative capability naturally locate on O2*p* and/or Ce^{3+}4*f* orbitals as shown in Scheme 2, and photoinduced electrons with reductive capability located on Ti3*d* and Ce5*d* orbitals. Because the CO_2 segment in m-CO_3^{2-} surface species is only connected with oxygen atoms of ceria and titania, it is difficult for them to be reduced to CO_2^-. However, the CO_2 segment in both b-HCO_3^- and b-CO_3^{2-} surface species is simultaneously bonded with oxygen and the Ti/Ce atom, enhancing the chance of being reduced to CO_2^- under photoillumination.

In order to further probe b-CO_3^{2-} photochemical reactivity, the FTIR spectra for CO_2 adsorption on the surface of 0.2 CeO_2/TiO_2 are supplied in Fig. 10. Unexpectedly, the peaks for b-CO_3^{2-} species show little change, and the CO_2^- species is not observed under simulated solar light irradiation. The results suggest that the b-CO_3^{2-} species is inactive without the presence of H_2O, in agreement with the theoretical calculation by Yin et al., which suggests that the presence of aqueous solutions can greatly decrease the energy barrier for the formation of CO_2^- species [60]. Besides, the energy barrier for the transfer of HCO_3^- to CO_2^- is about 0.27 eV, significantly lower than that of 0.87 eV for b-CO_3^{2-} to CO_2^- [56,60,63]. Based on these results, two possible routes for the conversion of surface b-CO_3^{2-} to CO_2^- species in the presence of H_2O are proposed: (i) b-CO_3^{2-} is activated by neighboring H_2O molecule on the surface, thus being transformed directly to CO_2^- species under light irradiation.

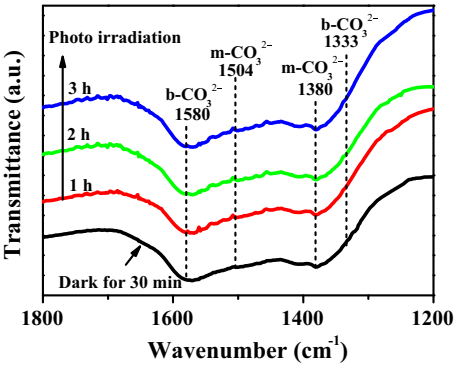

Fig. 10. In situ FTIR spectra for CO_2 adsorption on 0.2 CeO_2/TiO_2. The spectra were obtained after the exposure of 0.2 CeO_2/TiO_2 at room temperature to CO_2 followed by evacuation for 30 min before and after simulated solar light irradiation.

H_2O molecule could be bound to the oxygen of Ti–O–C in surface b-CO_3^{2-} through hydrogen bonding interaction [13], thus weakening the O–C bond. Sequentially, the C–O bond would be easily cleaved to form CO_2^- species with the assistance of photogenerated electrons. (ii) The H_2O molecule could be dissociated to form surface hydroxyls and hydrogen on the surfaces [65,66]. Once the surface H is bonded to O of surface b-CO_3^{2-}, b-HCO_3^- is then formed [54]. After that, the formed b-HCO_3^- is converted to CO_2^- species under light irradiation. Based on the results of FTIR and the formed products of CO_2 photoreduction, possible reaction pathways are proposed as follows:

$$H_2O \rightarrow H_{ads.} + OH_{ads.} \quad (1)$$

$$CO_2 + MO_2 \rightarrow CO_3^{2-} + MO^{2+} \text{ (M is denoted as Ti or Ce)} \quad (2)$$

$$CO_2 + OH + MO_2 \rightarrow HCO_3^- + MO_2^+ \quad (3)$$

$$HCO_3^- + h\nu \rightarrow CO_2^- + OH_{ads.} \quad (4)$$

$$CO_3^{2-} + MO^{2+} + H_{ads.} \rightarrow HCO_3^- + MO_2^+ \quad (5)$$

$$CO_3^{2-} + MO^{2+} + H_2O + h\nu \rightarrow CO_2^- + MO_2^+ + H_2O \quad (6)$$

$$CO_2^- + MO_2^+ + h\nu \rightarrow CO + MO_2 + O_{ads.} \quad (7)$$

$$O_{ads.} + 2H \rightarrow H_2O \quad (8)$$

$$O_{ads.} + O_{ads.} \rightarrow O_2 \quad (9)$$

$$CO \xrightarrow{e^-} C_{ads.} \xrightarrow{H} CH \xrightarrow{H} CH_3 \xrightarrow{H} CH_4. \quad (10)$$

3.5. Photoreduction of CO_2 in CO_2/H_2O (g)

The photocatalytic activities of TiO_2, 0.1 CeO_2/TiO_2, 0.2 CeO_2/TiO_2, 0.4 CeO_2/TiO_2, and CeO_2 catalysts were evaluated by the reduction of CO_2 with H_2O vapor under simulated sunlight irradiation (0.20 W cm^{-2}). In addition to oxygen, CO and CH_4 were found to be the major CO_2 reduction products, consistent with previous reports [67,68]. Fig. 11 shows the evolution of the main products (CO and CH_4) of CO_2 reduction with H_2O as a function of irradiation time over the photocatalysts under simulated sunlight irradiation. The yields of increase with irradiation time from 1 to 6 h for all five tested photocatalysts. At 6 h, the yield of CO is 30.6, 39.0, 46.6, 25.0, and 11.4 μmol g^{-1}, and the yield of CH_4 is 21.8, 19.4, 30.2, 20.6, and 8.8 μmol g^{-1} for TiO_2, 0.1 CeO_2/TiO_2, 0.2 CeO_2/TiO_2, 0.4 CeO_2/TiO_2, and CeO_2, respectively. In summary, the activity of photocatalysts increases with the increase of CeO_2 content and reaches maxima at 20 wt.% CeO_2 content. After that, the activity decreases with further increasing CeO_2 contents. The performance of bared TiO_2 is significantly higher than that of CeO_2 under simulated sunlight irradiation, suggesting that TiO_2 is the main active composition, while CeO_2 acts as a promoter in the CeO_2/TiO_2 photocatalysts.

In addition, three control experiments were performed: (1) irradiation of catalyst and H_2O vapor with visible light in the absence of CO_2; (2) visible-light irradiation of CO_2 and H_2O in the absence of catalyst; and (3) irradiation of catalyst and CO_2 without H_2O vapor. CO and CH_4 products were not monitored by gas phase analysis in the latter two experiments, confirming the photocatalytic conversion of CO_2.

According to the microcalorimetric measurement and in situ FTIR results, it is reasonable to conclude that the presence of CeO_2 containing Ce^{3+} not only increases the ability to capture reactant CO_2 molecules on the catalyst surface, but also facilitates the

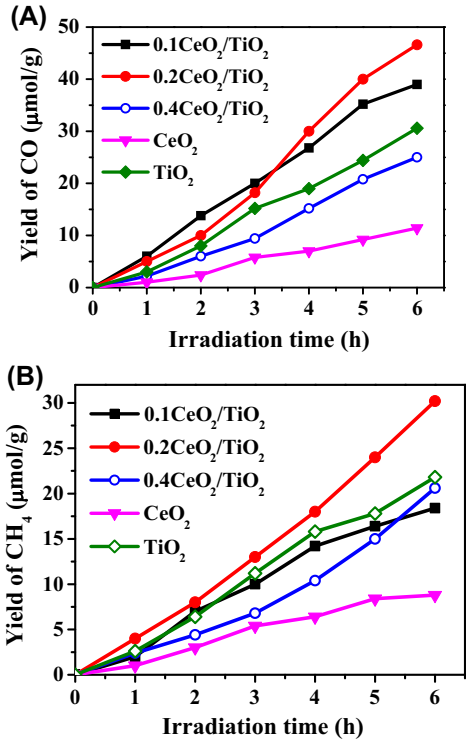

Fig. 11. Yields of CO (A) and CH_4 (B) products for CO_2 photoreduction as a function of irradiation time over the TiO_2, 0.1 CeO_2/TiO_2, 0.2 CeO_2/TiO_2, 0.4 CeO_2/TiO_2 and CeO_2 photocatalysts under simulated light irradiation.

production of b-HCO_3^- and b-CO_3^{2-} species that are active and could readily be transformed to CO_2^- intermediate in CO_2 photocatalytic reduction. Furthermore, the photogenerated charge separation efficiency of catalysts is obviously enhanced in CeO_2/TiO_2 hybrid catalysts, as evidenced by the results of transient photocurrent measurements. This could be responsible for the enhanced activity of CeO_2/TiO_2 hybrid catalysts with relatively low ceria content, such as 20%. On the other hand, because the intrinsic photocatalytic activity of as-prepared CeO_2 in the work is obviously lower than that of TiO_2, further increasing the ceria content in CeO_2/TiO_2 hybrid catalysts inevitably leads to a decrease in activity.

4. Conclusions

Highly dispersed CeO_2-on-TiO_2 photocatalysts were facilely prepared by a one-pot hydrothermal method. The addition of CeO_2 extends the light absorption of the resultant photocatalyst to the visible region and facilitates the photogenerated charge separation, which could be attributed to the presence of Ce^{3+} in CeO_2/TiO_2 hybrids.

Monodentate carbonate (m-CO_3^{2-}), bidentate carbonate (b-CO_3^{2-}), and bidentate bicarbonate (b-HCO_3^-) are found to be the main surface species for the coadsorption of CO_2 and H_2O on the surface of TiO_2 and CeO_2/TiO_2. The presence of CeO_2 containing Ce^{3+} strengthens the bonding of CO_2 with the photocatalyst's surface and increases the production of b-CO_3^{2-} and b-HCO_3^- surface species. Unlike m-CO_3^{2-}, both b-CO_3^{2-} and b-HCO_3^- surface species could be readily transformed to surface CO_2^- in the presence of H_2O under simulated sunlight irradiation. For the first time, it is experimentally demonstrated that the CO_2^- surface species is derived from b-CO_3^{2-} and b-HCO_3^- but not from gaseous and physisorbed CO_2 molecules.

The factor dominating the rate of CO_2 photoreduction under simulated sunlight irradiation is changed with increasing CeO_2 content. Ceria-tuned CO_2 adsorption and enhanced charge separation efficiencies are most likely to be responsible for the increased activity of hybrid catalysts with lower CeO_2 content, such as 20 wt. %. However, the presence of CeO_2 becomes detrimental for the activity at higher loadings, due to the fact that the intrinsic activity of CeO_2 is significantly lower than that of TiO_2 under simulated sunlight irradiation.

Acknowledgments

Financial support by the National Nature Science Foundation of China (Grant No. 21473248), the CAS Hundred Talents Program, the CAS-SAFEA International Partnership Program for Creative Research Teams, and the CAS "Western Light" Program (XBBS201408) is gratefully acknowledged.

Appendix A. Supplementary material

Supplementary data associated with this article can be found, in the online version, at http://dx.doi.org/10.1016/j.jcat.2015.12.030.

References

[1] L. Liu, H. Zhao, J.M. Andino, Y. Li, ACS Catal. 2 (2012) 1817–1828.
[2] A. Corma, H. Garcia, J. Catal. 308 (2013) 168–175.
[3] L. Liu, C. Zhao, D. Pitts, H. Zhao, Y. Li, Catal. Sci. Technol. 4 (2014) 1539–1546.
[4] Y. Liu, S. Zhou, J. Li, Y. Wang, G. Jiang, Z. Zhao, B. Liu, X. Gong, A. Duan, J. Liu, Y. Wei, L. Zhang, Appl. Catal. B 168–169 (2015) 125–131.
[5] D.O. Scanlon, C.W. Dunnill, J. Buckeridge, S.A. Shevlin, A.J. Logsdail, S.M. Woodley, C.R.A. Catlow, M.J. Powell, R.G. Palgrave, I.P. Parkin, G.W. Watson, T. W. Keal, P. Sherwood, A. Walsh, A.A. Sokol, Nat. Mater. 12 (2013) 798–801.
[6] J. Buckeridge, K.T. Butler, C.R.A. Catlow, A.J. Logsdail, D.O. Scanlon, S.A. Shevlin, S.M. Woodley, A.A. Sokol, A. Walsh, Chem. Mater. 27 (2015) 3844–3851.
[7] B. Mei, A. Pougin, J. Strunk, J. Catal. 306 (2013) 184–189.
[8] G. Halasi, I. Ugrai, F. Solymosi, J. Catal. 281 (2011) 309–317.
[9] X. Meng, S. Ouyang, T. Kako, P. Li, Q. Yu, T. Wang, J. Ye, Chem. Commun. 50 (2014) 11517–11519.
[10] S. Xie, Y. Wang, Q. Zhang, W. Fan, W. Deng, Y. Wang, Chem. Commun. 49 (2013) 2451–2453.
[11] J. Zhao, H. Chen, X. Tian, H. Zang, Y. Fu, J. Shen, J. Catal. 298 (2013) 161–169.
[12] Q. Li, L. Zong, C. Li, J. Yang, Appl. Surf. Sci. 319 (2014) 16–20.
[13] M.A. Henderson, Surf. Sci. 400 (1998) 203–219.
[14] X. Lin, Z.T. Wang, I. Lyubinetsky, B.D. Kay, Z. Dohnalek, Phys. Chem. Chem. Phys. 15 (2013) 6190–6195.
[15] R.S. Smith, Z. Li, L. Chen, Z. Dohnálek, B.D. Kay, J. Phys. Chem. B 118 (2014) 8054–8061.
[16] L. Liu, C. Zhao, H. Zhao, D. Pitts, Y. Li, Chem. Commun. 49 (2013) 3664–3666.
[17] B. Zhao, Y.X. Pan, C.J. Liu, Catal. Today 194 (2012) 60–64.
[18] Y. Wang, B. Li, C. Zhang, L. Cui, S. Kang, X. Li, L. Zhou, Appl. Catal. B 130–131 (2013) 277–284.
[19] C. Gionco, M.C. Paganini, S. Agnoli, A.E. Reeder, E. Giamello, J. Mater. Chem. A 1 (2013) 10918–10926.
[20] H. Eskandarloo, A. Badiei, M.A. Behnajady, Ind. Eng. Chem. Res. 53 (2014) 7847–7855.
[21] R. Marschall, Adv. Funct. Mater. 24 (2014) 2421–2440.
[22] S. Luo, T.D. Nguyen-Phan, A.C. Johnston-Peck, L. Barrio, S. Sallis, D.A. Arena, S. Kundu, W. Xu, L.F.J. Piper, E.A. Stach, D.E. Polyanskiy, E. Fujita, J.A. Rodriguez, S. D. Senanayake, J. Phys. Chem. C 19 (2015) 2669–2679.
[23] R. Gillen, S.J. Clark, J. Robertson, Phys. Rev. B 87 (2013) 125116.
[24] M.J. Muñoz-Batista, M.N. Gómez-Cerezo, A. Kubacka, D. Tudela, M. Fernández-García, ACS Catal. 4 (2014) 63–72.
[25] M.J. Muñoz-Batista, A. Kubacka, M.N. Gómez-Cerezo, D. Tudela, M. Fernández-García, Appl. Catal. B 140–141 (2013) 626–635.
[26] M.J. Muñoz-Batista, M. Fernández-García, A. Kubacka, Appl. Catal. B 164 (2015) 261–270.
[27] M. Zeng, Y. Li, M. Mao, J. Bai, L. Ren, X. Zhao, ACS Catal. 5 (2015) 3278–3286.
[28] L. Matějová, K. Kočí, M. Reli, L. Čapek, A. Hospodková, P. Peikertová, Z. Matěj, L. Obalová, A. Wach, P. Kuśtrowski, A. Kotarba, Appl. Catal. B 152–153 (2014) 172–183.
[29] H. Liu, M. Wang, Y. Wang, Y. Liang, W. Cao, Y. Su, J. Photochem. Photobiol. A 223 (2011) 157–164.
[30] J. Jiao, Y. Wei, Z. Zhao, J. Liu, J. Li, A. Duan, G. Jiang, Ind. Eng. Chem. Res. 53 (2014) 17345–17354.
[31] J. Saavedra, H.A. Doan, C.J. Pursell, L.C. Grabow, B.D. Chandler, Science 345 (2014) 1599–1602.
[32] A. Testino, I.R. Bellobono, V. Buscaglia, C. Canevali, M. D'Arienzo, S. Polizzi, R. Scotti, F. Morazzoni, J. Am. Chem. Soc. 129 (2007) 3564–3575.
[33] H.M. Cheng, J.M. Ma, Z.G. Zhao, L.M. Qi, Chem. Mater. 7 (1995) 663–671.
[34] J. Yang, D. Wang, H. Han, C. Li, Acc. Chem. Res. 46 (2013) 1900–1909.

[35] M.H. Yang, P.C. Chen, M.C. Tsai, T.T. Chen, I.C. Chang, H.T. Chiu, C.Y. Lee, CrystEngComm 16 (2014) 441–447.
[36] L. Liu, F. Gao, H. Zhao, Y. Li, Appl. Catal. B 134–135 (2013) 349–358.
[37] H. Zhao, L. Liu, J.M. Andino, Y. Li, J. Mater. Chem. A 1 (2013) 8209–8216.
[38] J. Zhuang, S. Weng, W. Dai, P. Liu, Q. Liu, J. Phys. Chem. C 116 (2012) 25354–25361.
[39] J.P. Holgado, R. Alvarez, G. Munuera, Appl. Surf. Sci. 161 (2000) 301–315.
[40] X. Gao, Y. Jiang, Y. Zhong, Z. Luo, K. Cen, J. Hazard. Mater. 174 (2010) 734.
[41] G. Li, D. Zhang, J.C. Yu, Phys. Chem. Chem. Phys. 11 (2009) 3775–3782.
[42] Z. Zhang, Z. Zhou, S. Nie, H. Wang, H. Peng, G. Li, K.J. Chen, Power Sources 267 (2014) 388–393.
[43] J. Fang, X. Bi, D. Si, Z. Jiang, W. Huang, Appl. Surf. Sci. 253 (2007) 8952–8961.
[44] A.C. Johnston-Peck, S.D. Senanayake, J.J. Plata, S. Kundu, W. Xu, L. Barrio, J. Graciani, J.F. Sanz, R.M. Navarro, J.L.G. Fierro, E.A. Stach, J.A. Rodriguez, J. Phys. Chem. C 117 (2013) 14463–14471.
[45] S. Kundu, J. Ciston, S.D. Senanayake, D.A. Arena, E. Fujita, D. Stacchiola, L. Barrio, R.M. Navarro, J.L.G. Fierro, J.A. Rodriguez, J. Phys. Chem. C 116 (2012) 14062–14070.
[46] P.J. Hay, R.L. Martin, J. Uddin, G.E. Scuseria, J. Chem. Phys. 125 (2006) 034712-7.
[47] A.V. Prokofiev, A.I. Shelykh, B.T. Melekh, J. Alloys Compd. 242 (1996) 41–44.
[48] H. Jiang, P. Rinke, M. Scheffler, Phys. Rev. B 86 (2012) 125115-13.
[49] J. Zhao, H. Chen, J. Xu, J. Shen, J. Phys. Chem. C 117 (2013) 10573–10580.
[50] J. Graciani, K. Mudiyanselage, F. Xu, A.E. Baber, J. Evans, S.D. Senanayake, D.J. Stacchiola, P. Liu, J. Hrbek, J.F. Sanz, J.A. Rodriguez, Science 345 (2014) 546–550.
[51] G. Finos, S. Collins, G. Blanco, E. del Rio, J.M. Cíes, S. Bernal, A. Bonivardi, Catal. Today 180 (2012) 9–18.
[52] J. Baltrusaitis, J. Schuttlefield, E. Zeitler, V.H. Grassian, Chem. Eng. J. 170 (2011) 471–481.
[53] K. Pokrovski, K.T. Jung, A.T. Bell, Langmuir 17 (2001) 4297–4303.
[54] L. Mino, G. Spoto, A.M. Ferrari, J. Phys. Chem. C 118 (2014) 25016–25026.
[55] M.M. Rodriguez, X. Peng, L. Liu, Y. Li, J.M. Andino, J. Phys. Chem. C 116 (2012) 19755–19764.
[56] H. He, P. Zapol, L.A. Curtiss, J. Phys. Chem. C 114 (2010) 21474–21481.
[57] P.M. Albrecht, D.E. Jiang, D.R. Mullins, J. Phys. Chem. C 118 (2014) 9042–9050.
[58] Z. Cheng, B.J. Sherman, C.S. Lo, J. Chem. Phys. 138 (2013) 014702-12.
[59] K.R. Hahn, M. Iannuzzi, A.P. Seitsonen, J. Hutter, J. Phys. Chem. C 117 (2013) 1701–1711.
[60] W.J. Yin, M. Krack, B. Wen, S.Y. Ma, L.M. Liu, J. Phys. Chem. Lett. 6 (2015) 2538–2545.
[61] D.C. Sorescu, J. Lee, W.A. Al-Saidi, K.D. Jordan, J. Chem. Phys. 137 (2012) 074704-16.
[62] S. Zhu, S. Liang, Y. Tong, X. An, J. Long, X. Fu, X. Wang, Phys. Chem. Chem. Phys. 17 (2015) 9761–9770.
[63] H. He, P. Zapol, L.A. Curtiss, Energy Environ. Sci. 5 (2012) 6196–6205.
[64] N.M. Dimitrijevic, B.K. Vijayan, O.G. Poluektov, T. Rajh, K.A. Gray, H. He, P. Zapol, J. Am. Chem. Soc. 133 (2011) 3964–3971.
[65] C. Di Valentin, A. Tilocca, A. Selloni, T.J. Beck, A. Klust, M. Batzill, Y. Losovyj, U. Diebold, J. Am. Chem. Soc. 127 (2005) 9895–9903.
[66] P. Dementyev, K.H. Dostert, F. Ivars-Barceló, C.P. O'Brien, F. Mirabella, S. Schauermann, X. Li, J. Paier, J. Sauer, H.J. Freund, Angew. Chem. Int. Ed. 54 (2015) 13942–13946.
[67] X. Li, W. Li, Z. Zhuang, Y. Zhong, Q. Li, L. Wang, J. Phys. Chem. C 116 (2012) 16047–16053.
[68] Z. Zhang, Z. Wang, S.W. Cao, C. Xue, J. Phys. Chem. C 117 (2013) 25939–25947.